





Distributed control strategy for DC microgrids based on average consensus and fractional-order local controllers

Mehdi Doostinia¹  | Mohammad T. H. Beheshti¹  | Seyed A. Alavi²  |
Josep M. Guerrero³ 

¹Department of Electrical and Computer Engineering, Tarbiat Modares University, Tehran, Iran

²School of Electronic Engineering and Computer Science, Queen Mary University of London, London, UK

³Department of Energy Technology, Aalborg University, Aalborg, Denmark

Correspondence

Mohammad T. H. Beheshti, Faculty of Electrical and Computer Engineering, Tarbiat Modares University, Tehran, Iran.

Email: mbehesht@modares.ac.ir

Abstract

A novel distributed secondary layer control strategy based on average consensus and fractional-order proportional-integral (FOPI) local controllers is proposed for the regulation of the bus voltages and energy level balancing of the energy storage systems (ESSs) in DC microgrids. The distributed consensus protocol works based on an undirected sparse communication network. Fractional-order local controllers increase the degree of freedom in the tuning of closed-loop controllers, which is required for DC microgrids with high order dynamics. Therefore, here, FOPI local controllers are proposed for enhanced energy balancing of ESSs and improved regulation of the bus voltages across the microgrid. The proposed control strategy operates in both islanded and grid-connected modes of a DC microgrid. In both modes, the average voltage of the microgrid converges to the microgrid desired reference voltage. The charging/discharging of ESSs is controlled independent of the microgrid operating mode to maintain a balanced energy level. The performance of the proposed distributed control strategy is validated in a 38-V DC microgrid case study, simulated by Simulink real-time desktop, consisting of 10 buses and a photovoltaic renewable energy source.

1 | INTRODUCTION

A DC microgrid generally consists of distributed generations (DGs), energy storage systems (ESSs), and loads that work in both islanded and grid-connected modes [1–3].

In recent years, DC microgrids have found more applications and faster growth in power distribution networks. This is because of their advantages compared to their AC microgrid alternatives, such as the elimination of AC–DC conversion steps as well as the removal of reactive power. These advantages lead to energy loss reduction and economic component savings [4, 5]. The mainly used control strategies employed in microgrids can be categorised into the following three architectures [6–8]:

- Centralised control architecture
- Decentralised control architecture
- Distributed control architecture

In a centralised control system, there is a central controller that collects all the required data and processes it. Therefore, in

this strategy, the computation burden is on a single component, and the flexibility of the system is degraded, which makes it susceptible to a single point of failure [9, 10].

In a decentralised control system, controllers operate based on their local information. There are several controlling units in a decentralised control system such as converter controllers, load controllers, and DG controllers, among which there is no communication. The main disadvantages of this strategy are insufficient response time for load profile changes and steady-state voltage offsets. These shortages ultimately might lead to instability of the microgrid in certain scenarios [11–13]. In the distributed control strategies [14], the local information and the information from the neighbours over a sparse communication network are used by autonomous agents to achieve co-operative objectives.

Compared to centralised and decentralised control strategies, distributed control strategies provide better control performance with the cost of communication links. Some of the advantages of this strategy are scalability, robustness, reduction in computational complexity, high flexibility, no single point of

failure, and task distribution among the local controllers in the microgrids [15, 16]. Therefore, distributed control algorithms based on a communication network can provide a higher resiliency for microgrids [17–20].

Commonly proportional-integral-derivative (PID) controllers are used to regulate and control the local voltage in microgrids [21]. PID controllers are simple and have a better practical feasibility [22]. However, PID controllers pose low degrees of bandwidth, robustness, and freedom in tuneable parameters.

In recent years, with the introduction of the fractional calculus, fractional-order models have replaced traditional integer-order models. In this regard, the number of fractional-order models and their applications have rapidly grown [23, 24].

Fractional-order PID (FOPID) controllers have a higher degree of freedom in tuneable parameters because of the two extra adjustable parameters (λ , μ). A particular type of FOPID controller is the fractional-order PI (FOPI) controller discussed in [25, 26]. The FOPI controller has been introduced by $\left(\frac{k_i}{s^\lambda}\right)$ or $k_p\left(1 + \left(\frac{k_i}{s^\lambda}\right)\right)$. Compared to the traditional PI controllers, due to the introduction of the λ parameter, FOPI has one more degree of freedom [27–29]. Trial and error method is used to set the controller parameters in the majority of microgrid applications. For the new adjustable parameters of fractional controllers such as the FOPI controller, this method is also used to provide a lower steady-state error and higher bandwidth. In recent years, the number of fractional-order controllers used in microgrids has grown. In [29], a robust FOPID controller is used to control AC microgrid frequency. It was shown that a robust FOPID reduces the effects of PV and wind turbine output power fluctuations, load variations, and the parametric uncertainties of the islanded microgrid frequency. In [30], learning-based FOPID controllers are introduced and a decentralised demand response programming was proposed to mitigate the frequency deviation of a stand-alone microgrid because of parametric uncertainties as well as changes in climatic patterns. In [31], FOPID controllers were used in an islanded microgrid with a single power source to control the fluctuations of the output voltage. The controllers' performance was evaluated under specific load settings and it was shown that the proposed controller reduces the system voltage fluctuation.

Fractional-order controllers have the advantage of possessing more adjustable parameters, which allows fine-tuning of the control system to achieve better control performance and easier controller design due to higher degrees of freedom. This results in higher bandwidth for the supported frequency and more adjustable response time in the closed-loop system. For example, the traditional PI controller has two adjustable parameters, but the FOPI controller has three adjustable parameters. Here, we have followed a trial-and-error approach to tune the controller parameters which is a common approach for complex applications such as microgrids. Furthermore, due to the extra adjustable parameter of the FOPI controller used here, controller tuning has become

easier. In summary, the fractional-order controller has the following advantages:

- Achieves better performance, flexibility, and a higher degree of freedom in the controller design.
- Provides adjustable frequency and time responses and achieves robust performance as well as reduces high-frequency oscillations or chattering in the closed-loop system.

Several works have been reported regarding the use of distributed controllers for microgrids. In [32], distributed controllers were used to provide proportional current sharing for DC microgrids. In [33], a secondary layer controller was presented for accurate load sharing and voltage regulation in low voltage islanded microgrids. A hierarchical and distributed co-operative control strategy was presented in [34] for a networked microgrid. In [35], the authors have proposed a distributed resilience control strategy for multiple ESSs under fault and attack of secondary controllers. The proposed strategy gained to voltage and frequency restoration and state-of-charge (SoC) balancing under various faults. A semi consensus strategy has been proposed in [36] for multi-functional hybrid energy storage systems (HESSs) for DC microgrid. Conventional V–P droops are used to regulate the batteries in a HESS, and integral droops (IDs) are used to regulate the supercapacitors. With the semi-consensus approach, a generic mathematical modelling of HESS is developed.

To address the aforementioned issues, this study proposes a novel distributed secondary layer control strategy for DC microgrids, based on average consensus protocol and FOPI local controllers. The energy level of the ES systems is balanced in the distributed strategy over a sparse communication network. Then, the FOPI controllers are used in the feedback path of converter controllers. The performance of the proposed controller is verified by the simulation of a 10-bus case study 380 V DC microgrid using a Simulink real-time desktop.

The study is structured as follows: In Section 2, the DC microgrid configuration and its consisting components are discussed. In Section 3, an introduction to fractional-order PI controllers with the fractional calculus is provided. Then, in Section 4, the distributed average consensus protocol is discussed. The proposed distributed control framework is demonstrated in Section 5. In Section 6, the case study DC microgrid configuration is detailed along with the simulation results in Section 7. Finally, in Section 8, the conclusion of the study is provided.

2 | DC MICROGRID

The general configuration and structure of a DC microgrid are shown in Figure 1. Generally, there are four main components in a DC microgrid. These components are (1) DGs, (2) ESSs,

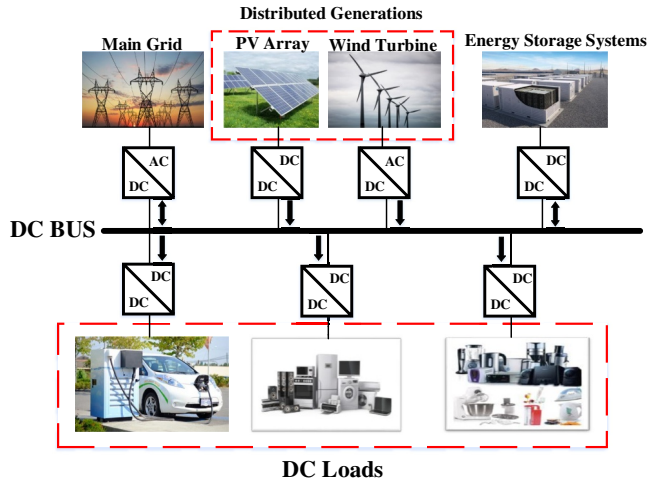


FIGURE 1 Components of a typical DC microgrid. It consists of DGs, DC loads, and AC–DC/DC–DC converters. DG, distributed generation

(3) power electronic converters, and (4) DC loads [37]. These items are detailed as follows:

1. Distributed generation: Photovoltaic (PV) generations and wind turbines are the commonly installed DGs. DGs are connected to the main bus with power electronic converters. PV generations have DC output and are connected to the central DC bus with DC–DC converters, whereas wind turbines have AC output and are connected to the central DC bus with AC–DC converters.
2. ES systems: The main devices that are widely used as ES systems are supercapacitors, electromechanical batteries, Li-ion batteries, and flywheels. Because of their natural DC output characteristic, they are usually integrated in DC microgrids with low-cost DC–DC converters. Load fluctuation causes rapid changes in voltage; therefore, the principal duty of ES systems is to compensate for these quick fluctuations.
3. Power electronic converters: Generally, DC–DC converters and AC–DC converters are used in DC microgrids for the interconnection of DGs and loads. For example, the main grid is connected to the main DC bus with the bidirectional AC–DC converters, and the ES systems and DC loads are connected to the same bus with DC–DC converters.
4. DC loads: DC loads are connected to the main DC bus at the appropriate voltage with DC–DC converters. In the case of multi-level DC systems, the corresponding voltage rated loads can be connected in the same way. DC loads include laptops, TV, washing machine, dryer, and so on.

DC microgrids operate in two modes: grid-connected mode and islanded mode. Here, the proposed controller works independently of the microgrid operating mode, which is evaluated in the simulation results. To guarantee maximum power absorption of the distributed energy resources such as PV panels, it is assumed that their converters work according to the maximum power point tracking scheme.

Here, the concept of virtual ESSs is used to integrate both DGs and ESSs in a single bus. This means that ESS acts as a buffer between the DG and the microgrid bus. Therefore, it is assumed that all the DGs have an internal ESS and have a series connection to the coupling bus. This removes the control complexity for the parallel operation of DGs and ESSs and provides a straightforward abstraction for the control system design.

3 | FRACTIONAL-ORDER CONTROLLER

3.1 | Introduction of fractional-order calculus

The integrodifferential operator in continuous time with order $\alpha \in \mathbb{R}^+$ is denoted in Equation (1). Fractional calculus is developed as an extension of ordinary integration/differentiation for non-integer order operators ${}_a \mathfrak{D}_t^\alpha$, where a and t exhibit the operation bund.

$${}_a \mathfrak{D}_t^\alpha = \begin{cases} d^\alpha/dt^\alpha & \alpha > 0, \\ 1 & \alpha = 0, \\ \int_a^t (d\tau)^{-\alpha} & \alpha < 0, \end{cases} \quad (1)$$

The Euler's Gamma function is one of the primary and basic functions in fractional calculus and is defined as the following:

$$\Gamma(z) = \int_0^\infty e^{-t} t^{z-1} dt \quad (2)$$

The existing integral on the right side of Equation (2) converges to the values of the variable z for $z > 0$.

There are several integrodifferential operator definitions. The three well-known and common definitions are as follows:

- Riemann–Liouville definition.
- Grünwald–Letnikov definition.
- Caputo definitions.

The Riemann–Liouville integrodifferential is commonly defined as follows:

$${}_a \mathfrak{D}_t^\alpha f(t) = \frac{1}{\Gamma(m-\alpha)} \left(\frac{d}{dt} \right)^m \int_a^t \frac{f(\tau)}{(t-\tau)^{\alpha-m+1}} d\tau \quad (3)$$

where $m-1 < \alpha < m$, $m \in \mathbb{N}$, and $\Gamma(\cdot)$ is Euler's gamma function.

Likewise, the Grünwald–Letnikov is defined as follows:

$${}_a \mathfrak{D}_t^\alpha f(t) = \lim_{h \rightarrow 0} \frac{1}{h^\alpha} \sum_{j=0}^{\lfloor \frac{t-a}{h} \rfloor} (-1)^j \binom{\alpha}{j} f(t-jh) \quad (4)$$

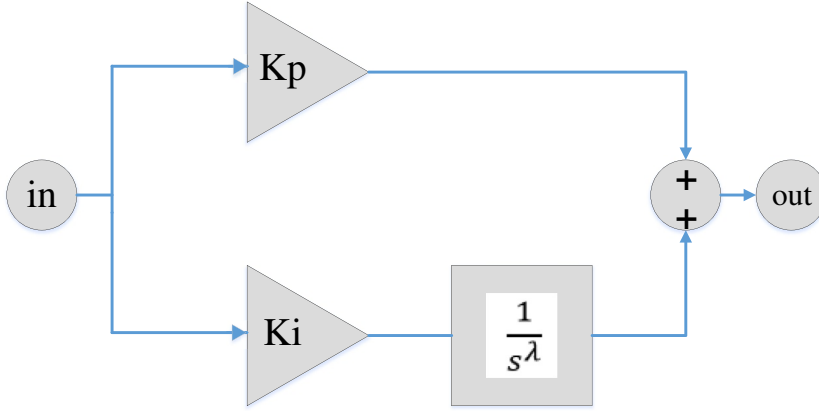


FIGURE 2 The structure of the fractional PI controller. λ defines the fractional-order of the PI controller. PI, proportional-integral

The Caputo definitions with a fractional-order of derivative α for a function $f: \mathbb{R}^+ \rightarrow \mathbb{R}$ is defined as the following [38]:

$${}_a \mathfrak{D}_t^\alpha = \begin{cases} \frac{1}{\Gamma(m-\alpha)} \int_a^t \frac{f^{(m)}(\tau)}{(t-\tau)^{\alpha-m+1}} d\tau & , m-1 < \alpha < m \\ \frac{d^m}{dt^m} f(t) & , \alpha = m \end{cases} \quad (5)$$

where m is the first integer greater than α .

With the lower boundary $a = 0$ and assuming zero initial condition, the Laplace transform of the α -th derivative of $f(t)$ is defined as follows: ($\alpha \in \mathbb{R}^+$):

$$\int_0^\infty e^{-st} {}_0 \mathfrak{D}_t^\alpha f(t) dt = s^\alpha F(s) \quad (6)$$

where $s = j$ is the Laplace transform parameter.

3.2 | Fractional-order PI controller

The proposed FOPI controller structure is shown in Figure 2.

The control law of the FOPI controller (PI^λ) in the time domain is as follows:

$$u(t) = K_p e(t) + K_i \cdot \int_t^\lambda e(t) \quad (7)$$

where λ component is the integral order and $e(t)$ is the error signal. The fractional-order signal is described as $\int_t^\alpha x(t) = D_t^{-\alpha} x(t)$. In the Laplace domain, the transfer function of the PI^λ controller is as follows:

$$C(s) = K_p + \frac{K_i}{s^\lambda}, \lambda_e \in (0, 2) \quad (8)$$

It is quite clear that the FOPI controller has three adjustable parameters K_p , K_i , λ while the classical PI controller intrinsically has solely two tuneable parameters K_p , K_i .

Therefore, it can be easily understood that the FOPI controller has an additional degree of freedom that can be tuned for optimised performance.

Considering Equation (8), if we put the lambda value equal to 1, the FOPI controller turns into a traditional PI controller. Hence, the classical PI controllers are special cases of the FOPI controllers.

4 | DISTRIBUTED CONSENSUS-BASED CONTROLLER

Here, every ES system has a consensus-based controller that uses its local measurements and the shared information from the neighbouring ES controllers to update its energy level (in per-unit) \bar{e}_i and the average voltage of the microgrid \bar{v}_i . Tracking the dynamic signals is the aim of this controller which is achieved by the following distributed average consensus protocol:

The distributed ES controllers are connected through a network communication graph $\mathcal{G}(\mathcal{V}, \mathcal{E})$, where $\mathcal{V} = \{1, \dots, N\}$ represents the nodes and \mathcal{E} represents the edges of the graph. Each node represents an ES controller and the edges represent the communication link between them. If there is a communication link between the nodes, they share information. The set of nodes connected to node i is called the neighbourhood of node i and is denoted by N_i . Each node has a nodal degree which is equal to the number of its neighbours and is denoted by $d_i = |N_i|$.

Every graph has a degree matrix D formed by d_i and an adjacency matrix A which is defined by $a_{ij} = 1$ if and only if $(i, j) \in \mathcal{E}$, and $a_{ij} = 0$ otherwise. $L = D - A$ is the Laplacian matrix of the graph. In undirected graphs, the Laplacian matrix has an eigenvalue equal to zero $0 = \lambda_{g1}(L) < \lambda_{g2}(L) \leq \dots \lambda_{gN}(L)$.

The i -th ES controller will receive the average estimated state from its neighbours. Thereafter, the controller estimator uses the following average consensus protocol:

$$\bar{x}_i(t) = x_i(t) + \int \sum_{j \in N_i} a_{ij} (\bar{x}_j - \bar{x}_i) \quad (9)$$

where x_i is a local state variable, and \bar{x}_i is a local average estimate of the shared value for the microgrid ES systems.

The distributed average consensus protocol has the following vector form dynamics:

$$\dot{\bar{\mathbf{x}}} = \dot{\mathbf{x}} - \mathbf{L}\bar{\mathbf{x}} \quad (10)$$

where $\mathbf{x} = [x_1, x_2, \dots, x_N]$ and $\bar{\mathbf{x}} = [\bar{x}_1, \bar{x}_2, \dots, \bar{x}_N]$.

By taking the Laplace transform from Equation (10), the transfer matrix of the distributed consensus protocol yields as follows [39]:

$$\mathbf{H}^{\text{avg}} = \frac{\bar{\mathbf{x}}}{\mathbf{x}} = \mathbf{s}(\mathbf{s}\mathbf{I}_N + \mathbf{L})^{-1} \quad (11)$$

where \mathbf{X} and $\bar{\mathbf{X}}$ are the Laplace transforms of \mathbf{x} and $\bar{\mathbf{x}}$ respectively.

For the average consensus protocol, the steady-state gain of a balanced communication graph with a sparse communication link is obtained by the following averaging operation:

$$\lim_{s \rightarrow 0} \mathbf{H}^{\text{avg}} = \mathbf{Q}, \text{ where } [\mathbf{Q}]_{ij} = \frac{1}{N} \quad (12)$$

For a vector of constant inputs, it can be shown by the final value theorem that the x converges to the steady-state average values \mathbf{x}^{ss} as follows:

$$\lim_{t \rightarrow \infty} \bar{\mathbf{x}}(t) = \lim_{s \rightarrow 0} \mathbf{H}^{\text{avg}} \lim_{s \rightarrow 0} \mathbf{X} = \mathbf{Q}\mathbf{x}^{\text{ss}} = \langle \mathbf{x}^{\text{ss}} \rangle \mathbf{1} \quad (13)$$

5 | DISTRIBUTED CONTROL STRATEGY

For the regulation of the converter voltage, a droop control is used to adjust the output reference voltage of v_i^* as follows:

$$v_i^* = v^{\text{mg}} - F_i r_i (i_i - u_i^{\bar{v}} - u_i^e) \quad (14)$$

It is clear that the droop control works based on the locally measured output currents i_i and microgrid voltage reference v^{mg} . Two additional regulation signals are added to the main droop control equation. One of them is $u_i^{\bar{v}}$, which is the voltage offset removal control signal and the other one is u_i^e , the energy balancing control signal. $u_i^{\bar{v}}$ is designed to control the average bus voltage of the microgrid and u_i^e is designed to balance the energy level of ES systems as well as to maintain an accurate load sharing. Also, r_i in the droop control formula is the virtual resistance. Generally, virtual resistance is designed for the ES systems to use all their maximum capacities P_i^{max} , which causes the microgrid voltage

to be maintained with minimum deviation Δv from the microgrid reference voltage v^{mg} .

$$r_i = \frac{\Delta v}{\frac{P_i^{\text{max}}}{v^{\text{mg}}}} \quad (15)$$

In a droop control system, the load power is eventually shared between the ES systems in inverse proportion to their virtual resistances r_i .

DC microgrids expose high-order harmonics due to the converters' switching. In order to remove the harmonics, a low-pass filter is commonly installed with a cancellation frequency of ω_i^c :

$$F_i = \frac{\omega_i^c}{s + \omega_i^c} \quad (16)$$

Current regulation is then achieved in two stages [40]. In the first stage, a proportional-integral (PI) controller G_i^v is used in Equation (17) to adjust the converter internal current reference to regulate the output voltage:

$$i_i^* = G_i^v (v_i^* - v_i), G_i^v = p_i^{vp} + \frac{p_i^{vi}}{s} \quad (17)$$

Then in the next stage, the current controller sets the pulse width modulation switching duty cycle to control the switching components of the converter for the output current regulation.

For the energy balancing regulation signal u_i^e , a PI controller with fractional-order in Equation (18) is applied to set the energy level value e_i to the average energy level estimate of ES systems. Because ES systems have different capacities, the energy level in per-unit is used in the computations:

$$u_i^e = G_i^e (e_i - \bar{e}_i), G_i^e = p_i^{ep} + \frac{p_i^{ei}}{s^\lambda} \quad (18)$$

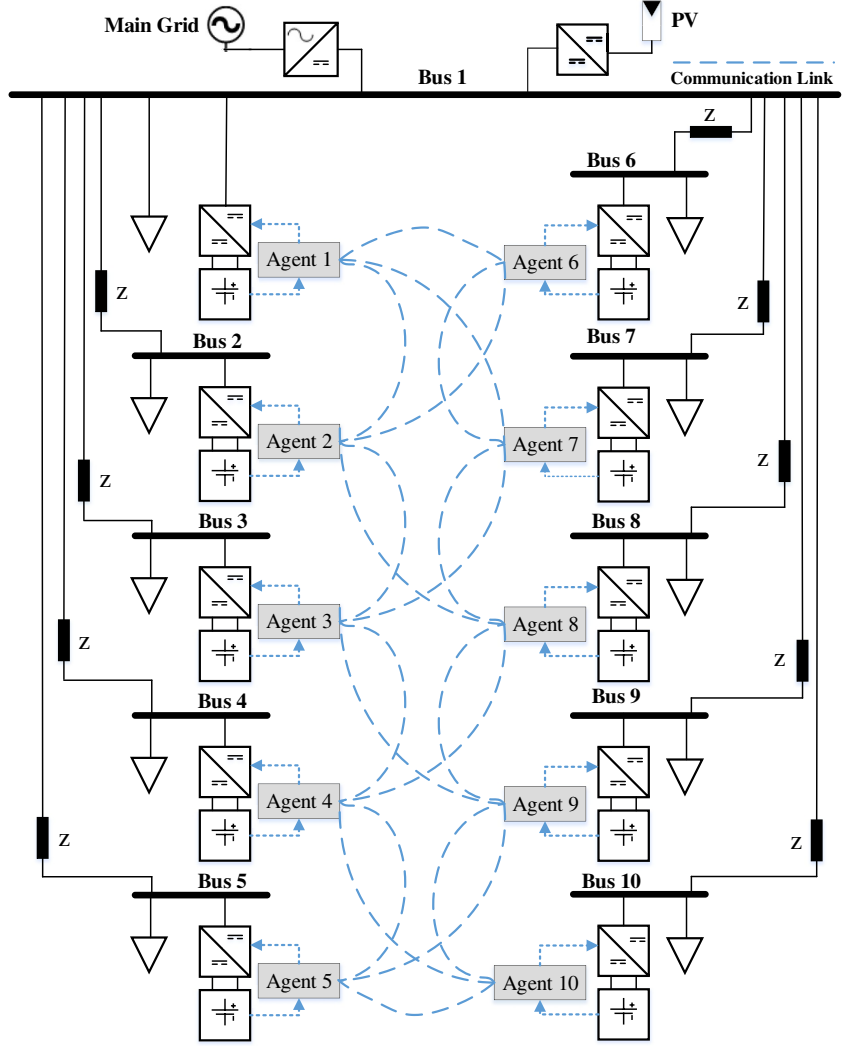
Also, for the voltage offset removal control signal $u_i^{\bar{v}}$, a fractional PI controller in Equation (19) is used, in which the local average bus voltage estimate is regulated to the microgrid reference voltage.

$$u_i^{\bar{v}} = G_i^{\bar{v}} (v^{\text{mg}} - \bar{v}_i), G_i^{\bar{v}} = p_i^{\bar{v}p} + \frac{p_i^{\bar{v}i}}{s^\lambda \bar{v}} \quad (19)$$

The block diagram of the control strategy is shown in Figure 3. The voltage dynamics of the system is then derived as a multiple-input multiple-output (MIMO) system. If V^{mg} is the Laplace transform of the microgrid voltage reference, the distributed control dynamics can be expressed as follows:

$$\mathbf{V}^* = \mathbf{V}^{\text{mg}} \mathbf{1} - \text{Fr} \left(\mathbf{I} - \mathbf{G}^{\bar{v}} (\mathbf{V}^{\text{mg}} \mathbf{1} - \bar{\mathbf{V}}) - \mathbf{G}^e (\mathbf{E} - \bar{\mathbf{E}}) \right) \quad (20)$$

FIGURE 5 The reference 10-bus DC microgrid for the case study. Communication links are established between the bus controller agents



The output current of the ES systems and bus voltages are related to the admittance matrix which is computed based on the microgrid lines and load impedances.

$$\mathbf{I} = \mathbf{YV} \quad (24)$$

A first-order linear model is also used for the energy level dynamics of the batteries [42].

$$\dot{e}_i = \frac{v_i t_i}{e_i^{\max}} \quad (25)$$

where e_i^{\max} is the highest capacity of the i -th ES system. Then, the global energy dynamics is derived as follows:

$$\mathbf{E} = \mathbf{MYV}, \mathbf{M} = \text{diag} \left\{ -\frac{v^{mg}}{e_i^{\max}} \right\} \quad (26)$$

Finally, the total closed-loop dynamics of the voltage regulation can be described by the following MIMO linear system:

TABLE 1 Value of loads' and batteries' capacity at each bus

Bus number	Batteries capacity (kWh)	Load power (kW)
Bus 1	25	15
Bus 2	25	15
Bus 3	25	15
Bus 4	25	15
Bus 5	25	15
Bus 6	25	5
Bus 7	25	5
Bus 8	12.5	5
Bus 9	12.5	5
Bus 10	12.5	5

$$\mathbf{V} = \left[\left(\mathbf{H}^{vcl} \right)^{-1} + \mathbf{FrG}^{\bar{v}} \mathbf{G}^{avg} - \mathbf{FrG}^e (\mathbf{I}_N - \mathbf{G}^{avg} \mathbf{MY})^{-1} V^{mg} (\mathbf{I}_N + \mathbf{FrG}^{\bar{v}}) \right] \quad (27)$$

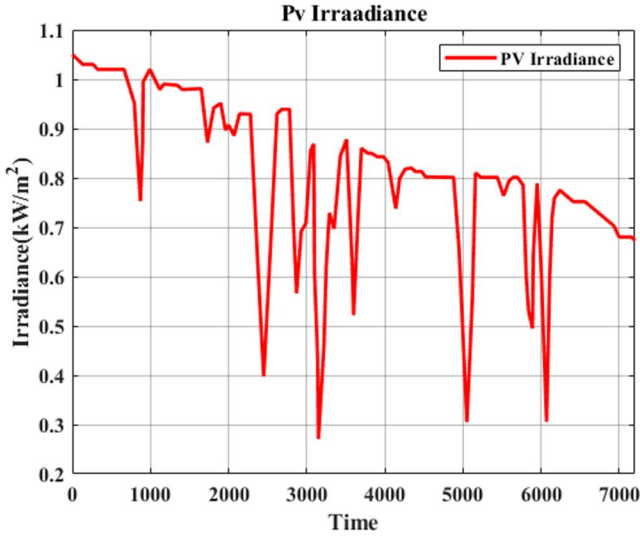


FIGURE 6 Irradiance data of the PV panel in the case study. PV, photovoltaic

6 | CASE STUDY MICROGRID

The 10-bus microgrid for the case study of this study is shown in Figure 5. A PV generation is connected to bus 1 as a DG with the interfacing DC–DC converter. Bus 1 is connected to the main grid with a 150 kW rated rectifier interfacing the connection. Each bus has a battery as the ES systems and is connected with a DC–DC converter to its corresponding bus. Each bus has a load with a different value. The connection impedances between the buses are designed by the analysis of wiring configurations in DC powered data centres, which are shown as Z in Figure 5.

The values of the loads in the buses and energy storage capacities are provided in Table 1. Buses 1–5 have 15 kW load and buses 6–10 have 5 kW load. Also, buses 1–7 have 25 kWh batteries and buses 8–10 have 12.5 kWh batteries. The PV generation was modelled based on the simulation approach from [43], using irradiance data from 2 PM to 4 PM on June 1, 2014, from the NREL Solar Radiation Research Laboratory (SRRL), Baseline Measurement System (BMS) in Colorado. The irradiance data of the PV panel is shown in Figure 6.

Virtual resistance is used in the droop control for power-sharing purpose; therefore, the power rating of ESSs is important for the calculation of resistance, not their energy capacity. In the scenario, we consider the maximum Δv to be equal to 3% for each bus. On the other hand, the voltage reference of the bus is equal to 380 V and $v^{mg} = 380v$. Therefore, $\Delta v = 0.03 \times 380 = 11.4$ V. P_i^{\max} is the maximum power of the batteries that are equal to the maximum power of the loads connected to each bus. The maximum loads' powers are shown in Table 1. Therefore, r_i is obtained as follows: $r_{1-5} = \frac{11.4}{\frac{15000}{380}} = 0.2888$ and $r_{6-10} = \frac{11.4}{\frac{5000}{380}} = 0.8663$

The battery ES system controllers are connected by a sparse bidirectional communication network. If there is no connection between the buses, the element of the adjacency

TABLE 2 Simulation parameters of the case study

Parameters	Value	Parameters	Value
R_{dc}	36 m Ω	ω_i^c	rad
L_{dc}	7 μ H	p_i^{cp}	50
r_{1-5}	0.2888	p_i^{ci}	100
r_{6-10}	0.8663	λ_e	0.7
Voltage	380	\bar{p}_i^{cp}	5
p_i^{cp}	10	\bar{p}_i^{ci}	20
p_i^{ci}	10	λ_v	1.5

matrix is 0; in contrast, if there is a connection between buses, the element of the adjacency matrix is 1.

For better demonstration, the communication link between the agents in the proposed control strategy is shown in Figure 7.

Also, the Laplacian matrix and their eigenvalue according to Figure 7 for the case study are as follows:

$$L = \begin{bmatrix} 3 & -1 & 0 & 0 & 0 & -1 & -1 & 0 & 0 & 0 \\ -1 & 4 & -1 & 0 & 0 & -1 & 0 & -1 & 0 & 0 \\ 0 & -1 & 4 & -1 & 0 & 0 & -1 & 0 & -1 & 0 \\ 0 & 0 & -1 & 4 & -1 & 0 & 0 & -1 & 0 & -1 \\ 0 & 0 & 0 & -1 & 3 & 0 & 0 & 0 & -1 & -1 \\ -1 & -1 & 0 & 0 & 0 & 3 & -1 & 0 & 0 & 0 \\ -1 & 0 & -1 & 0 & 0 & -1 & 4 & -1 & 0 & 0 \\ 0 & -1 & 0 & -1 & 0 & 0 & -1 & 4 & -1 & 0 \\ 0 & 0 & -1 & 0 & -1 & 0 & 0 & -1 & 4 & -1 \\ 0 & 0 & 0 & -1 & -1 & 0 & 0 & 0 & -1 & 3 \end{bmatrix} \quad (28)$$

with the eigenvalues as

$$\lambda_{g1} = 0, \lambda_{g2} = 0.7639, \lambda_{g3} = 2.7639, \lambda_{g4} = 4, \lambda_{g5} = 4, \lambda_{g6} = 4, \lambda_{g7} = 4, \lambda_{g8} = 4, \lambda_{g9} = 5.2361, \lambda_{g10} = 7.2361 \quad (29)$$

By definition, the sum of every row in the Laplacian matrix is zero. Therefore, the Laplacian matrix always has zero eigenvalue. This means that $rank(L) \leq n - 1$. For more explanation, the readers can refer to [44].

7 | SIMULATION RESULTS

We have considered the following scenario for the simulation of the proposed control strategy. In this scenario, the PV generation in specific periods is less than the power consumption of the microgrid, which is equal to 100 kW. In Figure 8, the PV generation power is shown. It is clear from

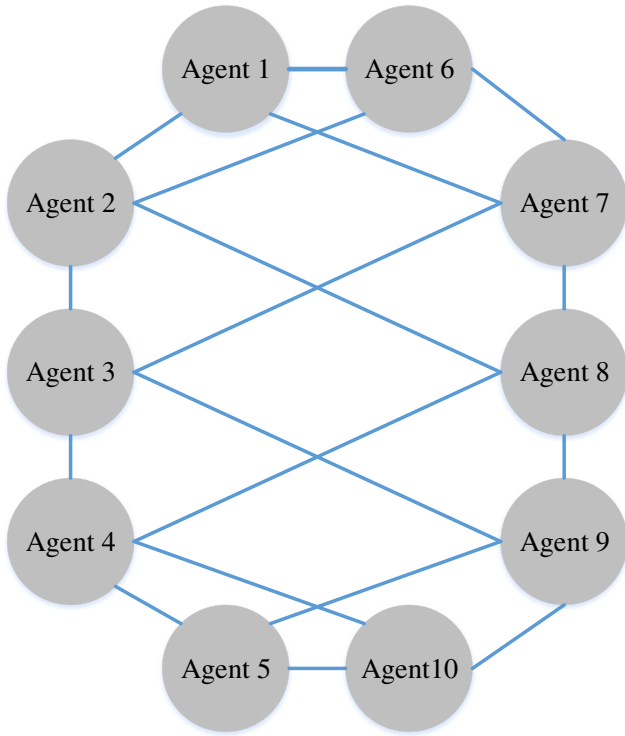


FIGURE 7 The undirected communication graph of the agents for the distributed average consensus protocol

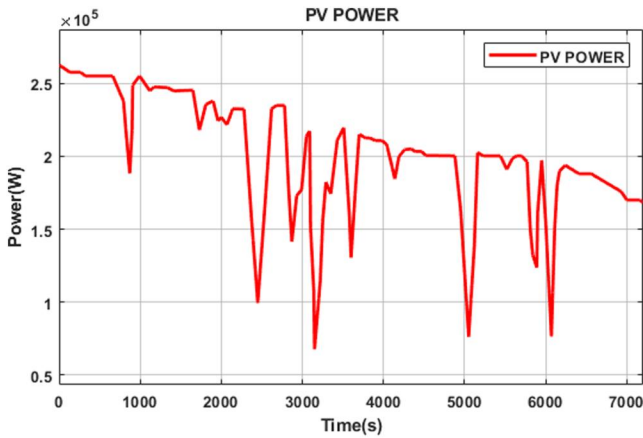


FIGURE 8 Injected PV power during the simulation in Watts. It has been calculated based on the information of the irradiance in Figure 6 and the size of the PV panels. PV, photovoltaic

Figure 9 that from 3100 to 3200 s, 5000 to 5100 s, and 6000 to 6100 s, the value of PV injected power is lower than 100 kW. Therefore, the PV cannot supply the excess microgrid load power. In this mode, the microgrid gets connected to the main grid. The main grid injects power to the microgrid, as shown in Figure 10. The value of main grid injected power is shown in Figure 10. In Figure 9, the voltage of buses under the proposed strategy is shown. Bus voltages reach the nominal voltage, 380 V, in less than 20 s.

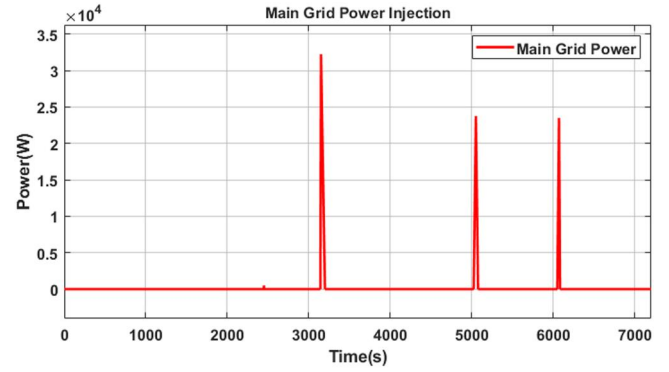


FIGURE 9 Main grid power injection in Watts during the simulation. When the PV panel supplied power was not enough, the main grid connection was established to supply the excess load power. PV, photovoltaic

During the operation, when the power of PV is less than load power (100 kW) in the highlighted periods, there is a transient variation in the voltage of buses. After the short-term variations, the bus voltages converge to 380 V very fast. This variation in the voltage is about 0.5 V, which is very low compared to the acceptable deviation in the literature, and it shows the proposed secondary control strategy provides acceptable performance. The simulation parameters are shown in Table 2.

The proposed controls strategy and the microgrid are simulated in MATLAB/Simulink using the real-time desktop toolbox and the Simscape toolbox.

The initial energy level of the ES systems per-unit are shown in Table 3. The energy level of ES systems per-unit during the simulation is also shown in Figure 11. As shown in Figure 11, every ES system starts from its initial value and charges completely in a very short time. When the PV power supply is less than the microgrid load (100 kW), the ES systems supply the excess load power as well as regulate the buses voltages. Also, the convergence of the energy level of each ES system can be seen clearly in the simulation, and it shows that the proposed secondary control strategy provides acceptable performance.

Here, the ESSs are used both as backup energy sources and also for stabilisation purposes. To fulfil both objectives at the same time, the ESSs need to be operated close to 1 p.u., which increases the microgrid reliability in the event of faults or disconnections in the microgrid. With this strategy, the microgrid can supply loads longer due to the fully charged backup ESSs. In Figure 12, the bus voltages' deviation from 380 V reference is shown. It is observable that the buses deviated voltage in different microgrid operation mode does not exceed 1 V. We set the allowed voltage deviation value of 3% of 380 V that equals to 11.4 V. It is clear that 0.5 V is a really small deviation compared to 11.4 V. Therefore, the deviation of voltage for each bus is less than the allowed value of the voltage deviation to maintain an acceptable power quality. This confirms the performance of the proposed distributed control strategy.

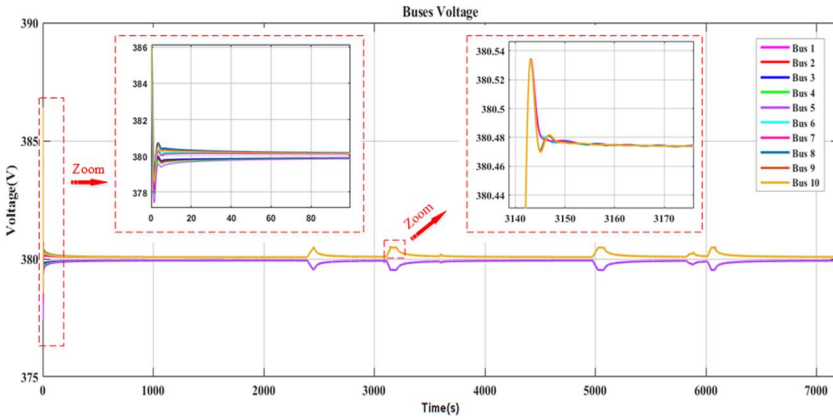


FIGURE 10 Voltage of buses during the simulation with the proposed distributed secondary layer control strategy. It can be seen that the voltage is stabilised around the nominal voltage of the microgrid (i.e. 380 V)

ES	Value	ES	Value
ES 1	0.5	ES 6	0.3
ES 2	0.6	ES 7	0.2
ES 3	0.7	ES 8	0.8
ES 4	0.4	ES 9	0.5
ES 5	0.1	ES 10	0.25

TABLE 3 Energy storage systems initial value for the simulation

Abbreviation: ES, energy storage.

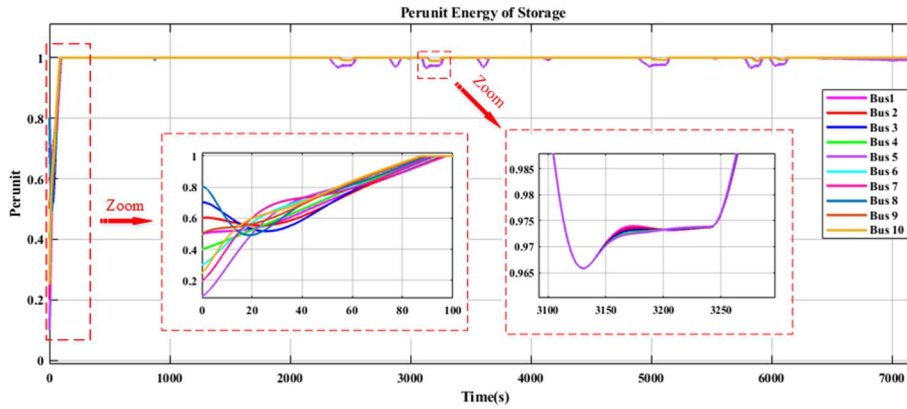


FIGURE 11 Per-unit energy level of ES systems during the simulation with the proposed distributed secondary layer control strategy. It can be seen that the energy level of the ES systems is balanced around 1 p.u. during the charging/discharging events. ES, energy storage

8 | CONCLUSION AND FUTURE WORK

This study proposed a novel distributed control strategy based on the average consensus protocol and FOPI local controllers for DC microgrids. The main objectives of this strategy are to stabilise the bus voltages and energy level balancing of the storage systems in a microgrid. This is realised by regulating the output voltage of the DC–DC converters. This strategy is able to control and regulate the microgrid output voltage and balance the energy level of the ES systems. The convergence speed of the energy levels as well as the convergence speed of the voltages has

shown an acceptable performance in both islanded and grid-connected modes of the microgrid operation. The existence of a fractional-order controller in the system causes the closed-loop system dynamics to become the fractional-order and the stability region of the fractional-order systems is larger than that of the integer order systems. Microgrid voltage stabilisation and low voltage offsets during mode transitions are the advantages of this strategy. For the future study, it is planned to use event-triggered distributed control strategies based on machine learning approaches to reduce the number of messages sent in the communications network.

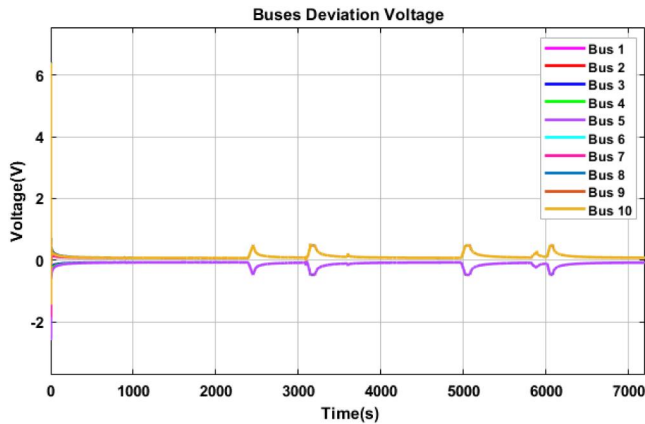


FIGURE 12 Deviation of the bus voltage from 380 V reference during the simulation. It can be seen that the deviation is minimised towards 0 due to the proposed secondary offset compensation controller

CONFLICT OF INTERESTS

The authors declare that there are no conflict of interests.

NOMENCLATURE

λ	integral order of FOPI controller.
k_i	integral gain of FOPI controller.
k_p	proportional gain of FOPI controller.
\mathcal{D}_t^α	non-integer operator.
$\Gamma(z)$	Euler's gamma function graph.
\mathcal{G}	communication graph.
\mathcal{V}	nodes of graph.
\mathcal{E}	edges of graph.
d_i	degree of the i -th node.
N_i	neighbours of i -th node.
A	adjacency matrix.
D	degree matrix.
L	Laplacian matrix.
λ_{gi}	eigenvalues of Laplacian matrix.
x_i	local state variable.
\bar{x}_i	local average estimate.
H^{avr}	transfer matrix of the distributed consensus protocol.
v^{mg}	microgrid voltage reference.
F_i	low-pass filter.
r_i	virtual resistance.
i	measured output current.
$u_i^{\bar{v}}$	control signal to remove voltage offset.
u_i^e	control signal to energy balancing regulation.
Δv	maximum voltage deviation.
ω_i^c	cancellation frequency.
G_i^v	PI controller to adjust converter internal current.
$p_i^{\bar{v}p}$	proportional gain of converter PI controller.
$p_i^{\bar{v}i}$	integral gain of converter PI controller.
G_i^e	FOPI controller to regulate energy level.
$p_i^{e\bar{p}}$	proportional gain of energy level's FOPI controller.
$p_i^{e\bar{i}}$	integral gain of energy level's FOPI controller.
$\lambda_{e\bar{v}}$	integral order of energy level's FOPI controller.
$G_i^{\bar{v}}$	FOPI controller to regulate buses' voltage

$\bar{p}_i^{\bar{v}p}$ proportional gain of buses voltage's FOPI controller.
 $\bar{p}_i^{\bar{v}i}$ integral gain of buses voltage's FOPI controller.
 $\lambda_{\bar{v}}$ integral order of buses voltage's FOPI controller.

ORCID

Mehdi Doostinia  <https://orcid.org/0000-0002-0022-304X>

Mohammad T. H. Bebeshti  <https://orcid.org/0000-0001-9863-0673>

Seyed A. Alavi  <https://orcid.org/0000-0003-2534-8866>

Josep M. Guerrero  <https://orcid.org/0000-0001-5236-4592>

REFERENCES

- Duan, J., et al.: Distributed control of inverter-interfaced microgrids with bounded transient line currents. *IEEE Trans. Ind. Inf.* 14(5), 2052–2061 (2018)
- Simpson, et al.: Voltage stabilisation in microgrids via quadratic droop control. *IEEE Trans. Autom. Control.* 62(3), 1239–1253 (2017)
- Gururaj, M.V., Padhy, N.P.: A novel decentralised coordinated voltage control scheme for distribution system with DC microgrid. *IEEE Trans. Ind. Inf.* 14(5), 1962–1973 (2018)
- Chen, D., Xu, L.: Autonomous DC voltage control of a DC microgrid with multiple slack terminals. *IEEE Trans. Power Syst.* 27(4), 1897–1905 (2012)
- Mohamad, A.M.E.I., Mohamed, Y.A.-R.I.: Investigation and assessment of stabilisation solutions for DC microgrid with dynamic loads. *IEEE Trans. Smart Grid.* 10(5), 5735–5747 (2019)
- Samad, T., Annaswamy, A.M.: Controls for smart grids: architectures and applications. *Proc. IEEE.* 105(11), 2244–2261 (2017)
- Doostinia, M., Bebeshti, M.T.H., Alavi, S.A.: A distributed control strategy with fractional order PI controller for DC microgrid. In: *Proceedings of the 2019 smart grid conference (SGC)*, pp. 1–6. Tehran (2019). <https://doi.org/10.1109/SGC49328.2019.9056587>
- Montazeri, M., et al.: Real time substation distributed control system simulator development based on IEC 61850 standard for a sample substation: case study: Sheikh Bahayi substation 400/230/63KV. In: *2013 Proceedings of the smart grid conference (SGC)*, pp. 108–112. Tehran (2013). <https://doi.org/10.1109/SGC.2013.6733820>
- Dörfler, F., Grammatico, S.: Gather-and-broadcast frequency control in power systems. *Automatica.* 79, 296–305 (2017)
- Fan, B., et al.: A consensus-based algorithm for power sharing and voltage regulation in DC microgrids. *IEEE Trans. Ind. Inf.* 16(6), 3987–3996 (2020)
- Alavi, S.A., et al.: An IoT-based data collection platform for situational awareness-centric microgrids. In: *Proceedings of the 2018 IEEE Canadian conference on electrical & computer engineering (CCECE)*, pp. 1–4. Quebec (2018). <https://doi.org/10.1109/CCECE.2018.8447718>
- Alavi, S.A., et al.: A distributed event-triggered control strategy for DC microgrids based on publish-subscribe model over industrial wireless sensor networks. *IEEE Trans. Smart Grid.* 10(4), 4323–4337 (2019)
- Alavi, S.A., Mehran, K., Hao, Y.: Optimal observer synthesis for microgrids with adaptive send-on-delta sampling over iot communication networks. *IEEE Trans. Ind. Electron.* 1 (2020)
- Lewis, F.L., et al.: *Cooperative Control of Multi-Agent Systems: Optimal and Adaptive Design Approaches*. Springer-Verlag, London (2014)
- Morstyn, T., Hredzak, B., Agelidis, V.G.: Control strategies for microgrids with distributed energy storage systems: an overview. *IEEE Trans. Smart Grid.* 9(4), 3652–3666 (2018)
- Morstyn, T., et al.: Unified distributed control for DC microgrid operating modes. *IEEE Trans. Power Syst.* 31(1), 802–812 (2016)
- Nasirian, V., et al.: Distributed adaptive droop control for DC distribution systems. *IEEE Trans. Energy Convers.* 29(4), 944–956 (2014)
- Baghaee, H.R., et al.: A decentralised power management and sliding mode control strategy for hybrid AC/DC microgrids including renewable energy resources. *IEEE Trans. Ind. Inf.* 1 (2017)

19. Fan, B., et al.: Output-constrained control of nonaffine multiagent systems with partially unknown control directions. *IEEE Trans. Autom. Control.* 64(9), 3936–3942 (2019)
20. Hossain, M.A., Pota, H.R.: Voltage tracking of a single-phase inverter in an islanded microgrid. *Int. J. Renew. Energy Res.* 5(3), 806–814 (2015)
21. Hadian, M., et al.: A new event-based PI controller using evolutionary algorithms. *J. Control Autom. Electr. Syst.* 30(6), 841–849 (2019)
22. Chen, Y.Q., et al.: Fractional-order control – a tutorial. *Proc. Am. Control Conf.* 1397–1411 (2009)
23. Tavazoei, M.S.: From traditional to fractional PI control: a key for generalisation. *IEEE Ind. Electron. Mag.* 6(3), 41–51 (2012)
24. Tepeljakov, A., et al.: Robust FOPI and FOPID controller design for FFOPDT plants in embedded control applications using frequency-domain analysis. *Proc. Am. Control Conf.* 3868–3873 (2015)
25. Wang, C., et al.: An analytical design of fractional-order proportional integral differential controller for robust velocity servo. In: *Proceedings of the 2013 25th Chinese control and decision conference (CCDC 2013)*, pp. 3359–3362. Guiyang (2013). <https://doi.org/10.1109/CCDC.2013.6561527>
26. Kadu, C.B., Patil, C.Y.: Performance assessment of IOPI and FOPI controller for FOPDT system. In: *Proceedings of the 2015 international conference on industrial instrumentation and control (IIC 2015)*, pp. 466–468. Pune (2015). <https://doi.org/10.1109/IIC.2015.7150787>
27. Bhambhani, V., Chen, Y.Q., Xue, D.: Optimal fractional-order proportional integral controller for varying time-delay systems. *IFAC Proc. Vol. (IFAC-PapersOnline)*. 17(1 Part 1) (2008)
28. Mahvash, H., et al.: Enhancement of DFIG performance at high wind speed using fractional-order PI controller in pitch compensation loop. *Int. J. Electr. Power Energy Syst.* 104, 259–268 (2019)
29. Khosravi, S., Hamidi Beheshti, M.T., Rastegar, H.: Robust control of islanded microgrid frequency using fractional-order PID. *Iran. J. Sci. Technol. - Trans. Electr. Eng.* 44(1) (2020)
30. Sikder, S.H., et al.: Fractional-Order Robust PID Controller Design for Voltage Control of Islanded Microgrid. In: *2018 4th International Conference on Electrical Engineering and Information & Communication Technology (ICEEICT)*, pp. 234–239. Dhaka (2018). <https://doi.org/10.1109/ICEEICT.2018.8628040>
31. Babaei, M., et al.: Coordination between demand response programming and learning-based FOPID controller for alleviation of frequency excursion of hybrid microgrid. *Energies*. 13(2) (2020)
32. Liu, Z., et al.: Stability analysis of DC microgrids with constant power load under distributed control methods. *Automatica*. 90, 62–72 (2018)
33. Golsorkhi, M.S., et al.: Distributed control of low-voltage resistive AC microgrids. *IEEE Trans. Energy Convers.* 34(2), 573–584 (2019)
34. Wu, X., et al.: A two-layer distributed cooperative control method for islanded networked microgrid systems. *IEEE Trans. Smart Grid.* 11(2), 942–957 (2020)
35. Lin, P., et al.: A semi-consensus strategy towards multi-functional hybrid energy storage system in DC microgrids. *IEEE Trans. Energy Convers.* 35(1), 336–346 (2020)
36. Deng, C., et al.: Distributed resilient control for energy storage systems in cyber-physical microgrids. *IEEE Trans. Ind. Inf.* 17(2), 1331–1341 (2021)
37. Lonkar, M., Ponnaluri, S.: An overview of DC microgrid operation and control. In: *IREC2015 The Sixth International Renewable Energy Congress* pp. 1–6. Sousse (2015). <https://doi.org/10.1109/IREC.2015.7110892>
38. Dadras, S., Momeni, H.R.: Control of a fractional-order economical system via sliding mode. *Phys. Stat. Mech. Appl.* 389(12), 2434–2442 (2010)
39. Nasirian, V., et al.: Distributed cooperative control of DC microgrids. *IEEE Trans. Power Electron.* 30(4), 2288–2303 (2015)
40. Mayo-Maldonado, J.C., et al.: Modelling and control of a DC-DC multilevel boost converter. *IET Power Electr.* 4(6), 693–700 (2011)
41. Chen, D., Xu, L., Yao, L.: DC network stability and dynamic analysis using virtual impedance method. In: *IECON 2012 - 38th Annual Conference on IEEE Industrial Electronics Society*, pp. 5625–5630. Montreal (2012). <https://doi.org/10.1109/IECON.2012.6389036>
42. Tanaka, T., et al.: Analysis of wiring design for 380-VDC power distribution system at telecommunication sites. In: *Intelec 2012*, pp. 1–5. Scottsdale (2012). <https://doi.org/10.1109/INTLEC.2012.6374529>
43. Villalva, M.G., Gazoli, J.R., Filho, E.R.: Comprehensive approach to modelling and simulation of photovoltaic arrays. *IEEE Trans. Power Electron.* 24(5), 1198–1208 (2009)
44. Olfati-Saber, R., Murray, R.M.: Consensus problems in networks of agents with switching topology and time-delays. *IEEE Trans. Autom. Control.* 49(9), 1520–1533 (2004)

How to cite this article: Doostinia M, Beheshti MTH, Alavi SA, Guerrero JM. Distributed control strategy for DC microgrids based on average consensus and fractional-order local controllers. *IET Smart Grid.* 2021;1–12. <https://doi.org/10.1049/stg2.12038>